

# Hybrid calibration of imaging sensors by neural networks and comparison with physical models

**David J. Lee**

Gas Technology Institute  
1700 South Mount Prospect Road  
Des Plaines, Illinois 60018-1800  
E-mail: David.Lee@gastechnology.org

**Soyoung S. Cha**, MEMBER SPIE

The University of Illinois at Chicago  
Department of Mechanical and  
Industrial Engineering  
Chicago, Illinois, 60607-7022  
E-mail: SSCha@uic.edu

**Abstract.** Imaging sensors have been deployed for a variety of noninvasive diagnostics in photogrammetry, videometry, and other pertinent gross-field visualization. Especially, three-dimensional (3-D) remote sensing based on stereoscopic vision has become increasingly important in many research and industrial applications. Typical applications can be particle tracking in flow visualization, motion/deformation detection in dynamics and stress analysis, and robot vision in automation and quality control, to name a few. The use of an appropriate calibration technique for image sensing is thus essential in both laboratory and field applications. To provide a robust and reliable calibration capability for stereoscopic 3-D detection, we develop a hybrid technique that is based on the use of artificial neural networks and a conventional physical-mathematical model. The hybrid technique is advantageous in procedural simplicity; that is, ease in hardware setup and speed in data processing. Our results show that the hybrid approach can improve the accuracy in predicting the object space coordinates by about 30% compared to those based on a purely physical-mathematical model. It appears that the hybrid technique can combine the merits of both physical-mathematical model and artificial neural networks to improve the overall performance. © 2006 Society of Photo-Optical Instrumentation Engineers. [DOI: 10.1117/1.2360938]

Subject terms: videometry; photogrammetry; three-dimensional vision; tracking velocimetry; gross-field displacement measurement.

Paper 050800R received Oct. 4, 2005; revised manuscript received Mar. 22, 2006; accepted for publication Mar. 31, 2006; published online Oct. 12, 2006.

## 1 Introduction

In gross-field metrology, devising a proper camera calibration procedure is essential to enhance overall measurement accuracy. Practically all image acquisition systems produce linear as well as nonlinear geometric distortions owing to imaging lens aberration, misalignment of optical components, imperfect sensor shape, etc. These deleterious effects alter both the relative and absolute positions of recorded images. The experimental setup can also cause distortions due to refractive-index change of media, including test-section walls, through which optical rays pass. These image distortions caused by both conceivable and inconceivable effects may lead to unacceptable measurement accuracy in quantitative photogrammetry and gross-field velocimetry. The erroneous effects can, however, be greatly minimized through proper calibration of the imaging system. In all imaging applications, it is thus very important to provide an accurate camera calibration procedure to achieve minimal errors in defining object positions. Previously, we have investigated three-dimensional (3-D) techniques of stereoscopic tracking velocimetry (STV) and also stereoscopic deformation mapping<sup>1,2</sup> (SDM). These techniques enable

simultaneously tracking of numerous artificial or naturally existing markers. The markers can be dispersed particles that move with a fluid in STV or dots that appear on an object surface in SDM. The conversion formula to be discussed here has been studied for these techniques, in order to relate the two two-dimensional (2-D) images to the 3-D absolute coordinate positions. Here, we thus discuss the camera calibration procedure in the context of STV and SDM; however, the generalization to other applications should be possible without modification.

Various physical-mathematical models (PMMs) exist for CCD image calibration. Tsai<sup>3</sup> presented the importance of a versatile camera calibration technique for off-the-shelf cameras. Existing literature as well as the advantages and disadvantages of each approach were discussed as well in the publication. Weng et al.<sup>4</sup> provided an excellent comparison of existing models for implementing a nonlinear

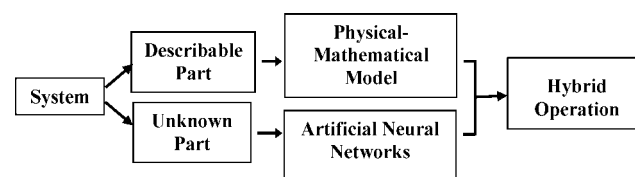


**Fig. 1** Description of the hybrid calibration scheme.

iterative scheme, which were devised to achieve enhanced accuracy in 3-D calibration. Choi and Guezennec<sup>5</sup> presented an *in situ* calibration scheme that relates the optical rays in an image volume directly to the points in each camera image plane. They claimed that the scheme not only increases the 3-D coordinate accuracy but also significantly reduces the computational time, as compared with conventional optical ray-tracing approaches. Recently, camera calibrations based on least-squares data fitting have been reported,<sup>1,2,6</sup> where a PMM is utilized based on the polynomial approximation of geometrical parameters in stereoscopic imaging. The technique appears not only to provide reliable capability for calibrating a volumetric field but also to be efficient to avoid the iterative corrections in a conventional scheme. However, further performance enhancement is desirable, especially for SDM applications where extreme accuracy is required.

Here, we present an approach for stereoscopic vision calibration based on artificial neural networks. The approach is based on the hybridization of artificial neural networks with a PMM to complement the weakness of the physical model. Building a PMM for system response is equivalent to finding a relationship between input and output for data extraction. The behavior of the system can be divided into two parts: that is, describable by the adopted PMM and indescribable or unknown in nature. The difference between the actual value and the PMM output can be the modeling error that corresponds to the latter. One of the important characteristics of artificial neural networks is that they are suitable for expressing the behavior of this unknown part of the system errors. Substantial research activities have been reported in the field of the feed-forward artificial neural networks that have been chosen for our calibration enhancement. The characteristics of the networks are that they can learn through training to approximate the system response and that they can predict the system behavior without using any explicit PMMs. Drawbacks, however, can be that a sufficient collection of known input/output responses is required for training the neural nets and that the training may involve a relatively long process to achieve satisfactory precision. By exploiting the merits of the two distinctive approaches, we expect the new hybrid concept to reduce errors in stereoscopic imaging.

## 2 PMM

Our approach is to first deploy a PMM with as much precision as possible. Feed-forward neural networks are then applied to further minimize the indescribable part of errors, as summarized in Fig. 1. Bethea et al.<sup>6</sup> introduced an efficient accurate PMM approach for 3-D calibration based on theoretical formulation of the imaging system. We believe that the approach is very reliable and efficient for practical implementation. The algorithm was thus adopted for the physical model in our hybrid approach. Here, we briefly present the essentials of the PMM concept as previously reported.<sup>1,2,6</sup> Let us install three coordinate systems: one for the absolute 3-D coordinates  $(X, Y, Z)$  of the field to be measured, and the other two for the 2-D image coordinates of  $(y_l, z_l)$  and  $(x_r, z_r)$  for the left and right cameras, respec-

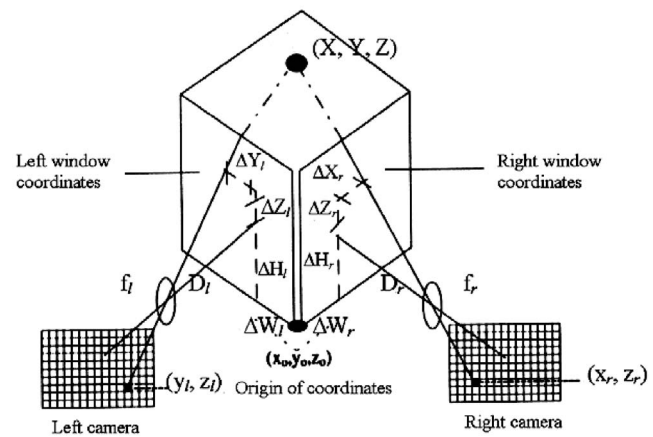


Fig. 2 Schematic for 3-D imaging.

tively. Even though images are captured in pixels, the 2-D image positions (centroids) of a marker in 3-D space can be found in fractional pixels through intensity weighting.<sup>1</sup> The goal of the camera calibration is to find the absolute 3-D position of  $(X, Y, Z)$  when its 2-D pixel positions of  $(y_l, z_l)$  and  $(x_r, z_r)$  are specified.

For simplicity, we define the origin of the 3-D coordinates at the lower front corner of the experimental volume or test setup chamber, between the two CCD cameras, as shown in Fig. 2. The origins of two image planes can be assumed at the center of each CCD sensor array. A ray of light that leaves a point  $(X, Y, Z)$ , i.e., trace marker, reaches pixel  $(y_l, z_l)$  on the CCD sensor after passing through the left imaging system. Similarly, another ray from the same point can reach pixel  $(x_r, z_r)$  of the right sensor. Also,  $D_l$  and  $D_r$  are effective distances from the left and right sensors to the left and right plane of the experimental volume, respectively. The symbols  $f_l$  and  $f_r$  represent the effective focal lengths of two cameras. The optical axis of the left camera strikes the left face of the experimental volume at  $(0, \Delta W_l, \Delta H_l)$ , while the right camera axis hits the right face at  $(\Delta W_r, 0, \Delta H_r)$ . The ray leaving the point toward the left camera crosses the left face of the chamber at  $(\Delta Y_l, \Delta Z_l)$  from the camera optical axis, while the ray to the right passes through the right face at  $(\Delta X_r, \Delta Z_r)$ . In calibration, the 3-D absolute coordinates  $(X, Y, Z)$  as well as the 2-D pixel coordinates  $(y_l, z_l)$  and  $(x_r, z_r)$  are known; however, in the stereoscopic measurements, we must find the former from the latter two. In the PMM calibration, the functional relationship must be determined between the absolute coordinates and pixel coordinates, which involves  $f_l, f_r, D_l, D_r, \Delta W_l, \Delta W_r, \Delta H_l$ , and  $\Delta H_r$  as parameters. In implementing our physical model, the two camera systems do not need to be positioned either at the same height or normally to the two side faces of the experimental volume.

By following the derivations, as discussed in previous investigations,<sup>1,2,6</sup> for the left imaging system, the  $Y$  and  $Z$  components of a point position can be modeled by Eq. (1), where the coefficients can be expressible in terms of the physical parameters as previously explained and shown in Fig. 2.

$$\begin{aligned}
Y \approx & A_0 + A_1 y_l + A_2 z_l + A_3 y_l X + A_4 z_l X + A_5 y_l |y_l| + A_6 y_l |z_l| + A_7 |y_l| z_l + A_8 z_l |z_l| + A_9 y_l (|y_l z_l|)^{1/2} + A_{10} z_l (|y_l z_l|)^{1/2} \\
& + A_{11} y_l |y_l| X + A_{12} y_l |z_l| X + A_{13} |y_l| z_l X + A_{14} z_l |z_l| X + A_{15} y_l (|y_l z_l|)^{1/2} X + A_{16} z_l (|y_l z_l|)^{1/2} X + A_{17} y_l^3 + A_{18} y_l^2 z_l \\
& + A_{19} y_l z_l^2 + A_{20} z_l^3 + A_{21} y_l^3 X + A_{22} y_l^2 z_l X + A_{23} y_l z_l^2 X + A_{24} z_l^3 X + \dots, \\
Z \approx & B_0 + B_1 y_l + B_2 z_l + B_3 y_l X + B_4 z_l X + B_5 y_l |y_l| + B_6 y_l |z_l| + B_7 |y_l| z_l + B_8 z_l |z_l| + B_9 y_l (|y_l z_l|)^{1/2} + B_{10} z_l (|y_l z_l|)^{1/2} \\
& + B_{11} y_l |y_l| X + B_{12} y_l |z_l| X + B_{13} |y_l| z_l X + B_{14} z_l |z_l| X + B_{15} y_l (|y_l z_l|)^{1/2} X + B_{16} z_l (|y_l z_l|)^{1/2} X + B_{17} y_l^3 + B_{18} y_l^2 z_l \\
& + B_{19} y_l z_l^2 + B_{20} z_l^3 + B_{21} y_l^3 X + B_{22} y_l^2 z_l X + B_{23} y_l z_l^2 X + B_{24} z_l^3 X + \dots.
\end{aligned} \tag{1}$$

Similarly, for the right imaging system,

$$\begin{aligned}
X \approx & C_0 + C_1 x_r + C_2 z_r + C_3 x_r Y + C_4 z_r Y + C_5 x_r |x_r| + C_6 x_r |z_r| + C_7 |x_r| z_r + C_8 z_r |z_r| + C_9 x_r (|x_r z_r|)^{1/2} + C_{10} z_r (|x_r z_r|)^{1/2} \\
& + C_{11} x_r |x_r| Y + C_{12} x_r |z_r| Y + C_{13} |x_r| z_r Y + C_{14} z_r |z_r| Y + C_{15} x_r (|x_r z_r|)^{1/2} Y + C_{16} z_r (|x_r z_r|)^{1/2} Y + C_{17} x_r^3 + C_{18} x_r^2 z_r \\
& + C_{19} x_r z_r^2 + C_{20} z_r^3 + C_{21} x_r^3 Y + C_{22} x_r^2 z_r Y + C_{23} x_r z_r^2 Y + C_{24} z_r^3 Y + \dots, \\
Z \approx & D_0 + D_1 x_r + D_2 z_r + D_3 x_r Y + D_4 z_r Y + D_5 x_r |x_r| + D_6 x_r |z_r| + D_7 |x_r| z_r + D_8 z_r |z_r| + D_9 x_r (|x_r z_r|)^{1/2} + D_{10} z_r (|x_r z_r|)^{1/2} \\
& + D_{11} x_r |x_r| Y + D_{12} x_r |z_r| Y + D_{13} |x_r| z_r Y + D_{14} z_r |z_r| Y + D_{15} x_r (|x_r z_r|)^{1/2} Y + D_{16} z_r (|x_r z_r|)^{1/2} Y + D_{17} x_r^3 + D_{18} x_r^2 z_r \\
& + D_{19} x_r z_r^2 + D_{20} z_r^3 + D_{21} x_r^3 Y + D_{22} x_r^2 z_r Y + D_{23} x_r z_r^2 Y + D_{24} z_r^3 Y + \dots.
\end{aligned} \tag{2}$$

In calibration, the known data points of  $(X, Y, Z)$  and the corresponding image pixel positions of  $(y_l, z_l)$  and  $(x_r, z_r)$  provide linear algebraic equations for determining the PMM coefficients in Eqs. (1) and (2). Here, the ordinary least-square method has been used to estimate the calibration coefficients. Practically, Eqs. (1) and (2) represent the equations of straight lines for the two rays emanating from a marker in 3-D space, which form images on the sensors. In a simplified form, they can be  $Y=a+bX$  and  $Z=a'+b'X$  for the left camera while  $Y=c+dX$  and  $Z=c'+d'X$  for the right camera. For an ideal case, the two rays should perfectly intersect at the marker position when obtained from the 2-D data of each camera. However, errors in measurement, modeling, and calibration cause the two rays deviate each other. For this reason, in our approach, the midpoint of the common normal to the two rays was taken as the estimate of the 3-D marker position.

We conducted computer simulation of experiments with assumed behaviors in optical imaging, aberration, misalignment, and sensor pixel size as well as with the perfectly accurate reference point position in imaging. Table 1 shows uncertainty of our PMM, where the object space measurement uncertainty was converted to the corresponding image space pixel values by multiplying the demagnification factor and dividing by the pixel size. The uncertainty in the table arises mostly from the truncation of the series in Eqs. (1) and (2). As seen, the truncation error is very negligible when the number of coefficients is greater than 11. Even those with 9 or 11 coefficients are acceptable. The measurement of the  $Z$  values is more accurate as compared to  $X$  and  $Y$  values. This is due to  $Z$  values could be captured by both of the cameras as seen in Fig. 2, allowing a redundancy in measurements. For real calibration experiments as summa-

rized in Table 2, Sony CCD sensors, Model XC-8500CE of  $782 \times 582$  pixels were utilized with an image demagnification factor of about 0.085. The calibration plate had circular grid markers of  $5 \pm 0.1$  mm spacing, whose centroid were used as known reference points in imaging. Here, the spacing uncertainty estimate is based on ruler measurement of only a few dot centers. It was extremely difficult to define the centers of the dots that were printed on a sheet. It could thus be an approximate estimate since the actual spacing might be more regular than the measured values. The plate was diagonally placed in the imaging volume with the two cameras orthogonally positioned. It was then moved back and forth by a known distance on a translation stage to generate stereoscopic images of about 320 dots.

**Table 1** Calibration results of stereoscopic imaging with computer-simulated data.

Number of Coefficients	Uncertainty in the X Position (pixels)	Uncertainty in the Y Position (pixels)	Uncertainty in the Z Position (pixels)
9	0.191	0.596	0.296
11	0.010	0.216	0.165
15	0.048	0.101	0.074
17	0.037	0.072	0.072
21	0.020	0.047	0.012
25	0.000	0.000	0.00

**Table 2** Calibration results of Stereoscopic Imaging with Real Data.

Number of Coefficients	Estimated Uncertainty in the X Position (pixels)	Estimated Uncertainty in the Y Position (pixels)	Estimated Uncertainty in the Z Position (pixels)
9	2.92	1.90	0.50
11	2.78	1.88	0.46
15	1.26	0.96	0.26
17	1.25	0.93	0.23
21	1.11	0.88	0.23
25	0.77	0.47	0.22

Knowing the relative positions of the reference calibration points and their camera's pixel positions, we could determine calibration coefficients. The uncertainty of marker spacing on the calibration plate corresponds to about 1 pixel on the sensor. We can thus reasonably expect that most of the uncertainty in the real experiments in Table 2 was originated from the inaccuracy in the marker marking and the uncertainty in the reference plate translation for calibration imaging. As expected,  $X$  and  $Y$  values resulted in better accuracy than  $Z$  values.

### 3 Hybridization with Neural Networks

PMMs in calibration provide only approximate positions of  $(X', Y', Z')$ , which can have biased or random errors, instead of accurate values of  $(X, Y, Z)$ . The biased errors including the series truncation is difficult to mathematically

describe but can be identified by applying artificial neural networks. The true position can then be denoted by

$$\begin{bmatrix} X \\ Y \\ Z \end{bmatrix} = \begin{bmatrix} X' \\ Y' \\ Z' \end{bmatrix} + \begin{bmatrix} \Delta x_p \\ \Delta y_p \\ \Delta z_p \end{bmatrix}. \quad (3)$$

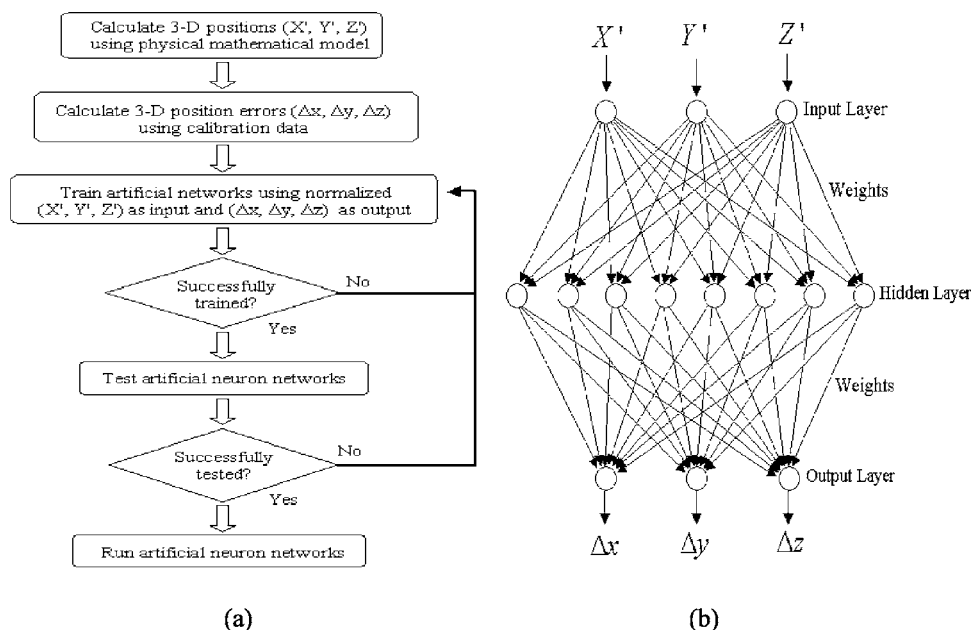
Here,  $(\Delta X_p, \Delta Y_p, \Delta Z_p)$  is the modeling error of the PMM in the calibration system. We used the feed-forward artificial neural networks<sup>7</sup> to estimate the modeling errors, as summarized in Fig. 3. It had three input, hidden, and output layers of 3, 8, and 3 neurons, respectively. The input to the net, that is, to the input layer, is the 3-D coordinates  $(X', Y', Z')$  of the object measured by the PMM. The output  $(\Delta X, \Delta Y, \Delta Z)$  from the output layer, which represents the responses of the network, estimates the modeling errors. These error estimates were used to correct the results from the PMM.

Let  $x_i$  be the  $i$ 'th output of the input layer,  $y_j$  is the  $j$ 'th output of the hidden layer, and  $z_k$  is the  $k$ 'th output of the output layer. The signals propagate forward from the input layer, to the hidden layer, and then to the output layer with the mechanism as

$$y_j = f \left( \sum_{i=1}^I w_{ij} x_i \right), \quad (4)$$

$$z_k = f \left( \sum_{j=1}^J w_{jk} y_j \right),$$

where  $w_{ij}$  is the weight (connection strength) between neuron  $i$  of the input layer and neuron  $j$  of the hidden layer, and  $I$  and  $J$  are the number of neurons in the input and hidden layers, respectively. The sigmoid function shown in

**Fig. 3** Hybrid calibration: (a) process structure and (b) feed-forward neural networks.

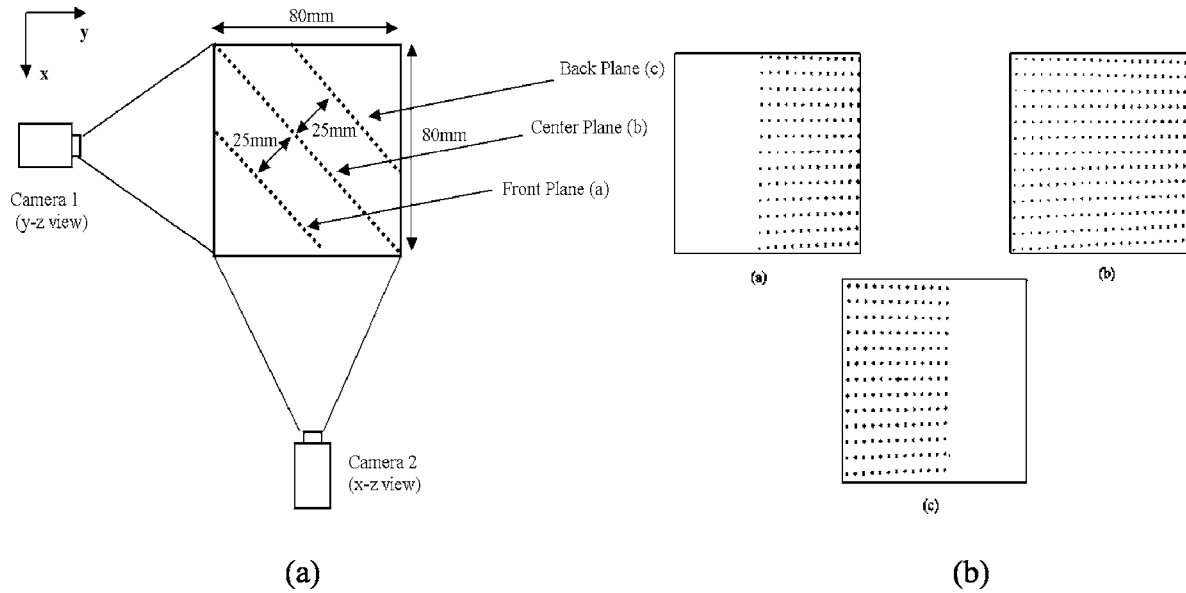


**Fig. 4** Experimental setup for testing the hybrid calibration technique: (a) schematic and (b) images of the calibration plate.

Eq. (5) was applied to an individual neuron as a transfer function where  $s$  is the resultant input to a neuron and  $f(s)$  is its output.

$$f(s) = \frac{1}{1 + e^{-s}}. \quad (5)$$

To produce proper output with given input, the network must be trained before application. For implementation, back-propagation (BP) was employed by presenting it with the known input and output pairs collected as samples for calibration. Let us briefly present the well-known principle of the BP algorithm.<sup>7</sup> For a total of  $P$  learning samples, let  $(x^1, x^2, \dots, x^P)$  be the input, let  $(t^1, t^2, \dots, t^P)$  be the target output (sample value), and let  $(z^1, z^2, \dots, z^P)$  be the actual output of the neural network with the input of the samples. For the  $P$  samples, the square sum of network errors, that is, the difference between the target output and actual output, can be expressed as

$$E = \frac{1}{2} \sum_{p=1}^P \sum_{k=1}^K (t_k^p - z_k^p)^2, \quad (6)$$

where  $K$  is the number of neurons in the output layer. The supervised learning involves an iterative procedure in which the samples are sequentially presented to the network in a repeated manner to alter connection weights between neurons until the network produces the optimal output for the given input. To do so, the network propagates the error backward, by altering the weights between two neurons in adjacent layers starting from the output layer toward the input layer. By using the gradient-descent method, the change in connection weights can be obtained by

$$\Delta w_{ij} = -\eta \frac{\partial E}{\partial w_{ij}}, \quad (7)$$

$$\Delta w_{jk} = -\eta \frac{\partial E}{\partial w_{jk}},$$

where  $\eta$  is the step size (learning rate) in each iteration. For the training, it can be shown that

$$\frac{\partial E}{\partial w_{jk}} = -\sum_{p=1}^P \delta_{jk}^p y_j^p, \quad (8)$$

$$\frac{\partial E}{\partial w_{ij}} = -\sum_{p=1}^P \delta_{ij}^p x_i^p,$$

where

$$\delta_{jk}^p = (t_k^p - z_k^p) z_k^p (1 - z_k^p), \quad (9)$$

$$\delta_{ij}^p = \sum_{k=1}^K \delta_{jk}^p w_{jk} y_j^p (1 - y_j^p).$$

After changing weights, when the samples are presented again as input to the network, a different output set is obtained due to the new connection weights  $w_{mn}$ . The change of errors is then

$$\Delta E = \sum_{mn} \frac{\partial E}{\partial w_{mn}} \Delta w_{mn} = -\eta \sum_{mn} \left( \frac{\partial E}{\partial w_{mn}} \right)^2 \leq 0. \quad (10)$$

As seen, the total error always decreases through iteration. The iteration continues until the error is reduced to a satisfactory level, which enables the actual output of the network to properly match the target output. At this point, the



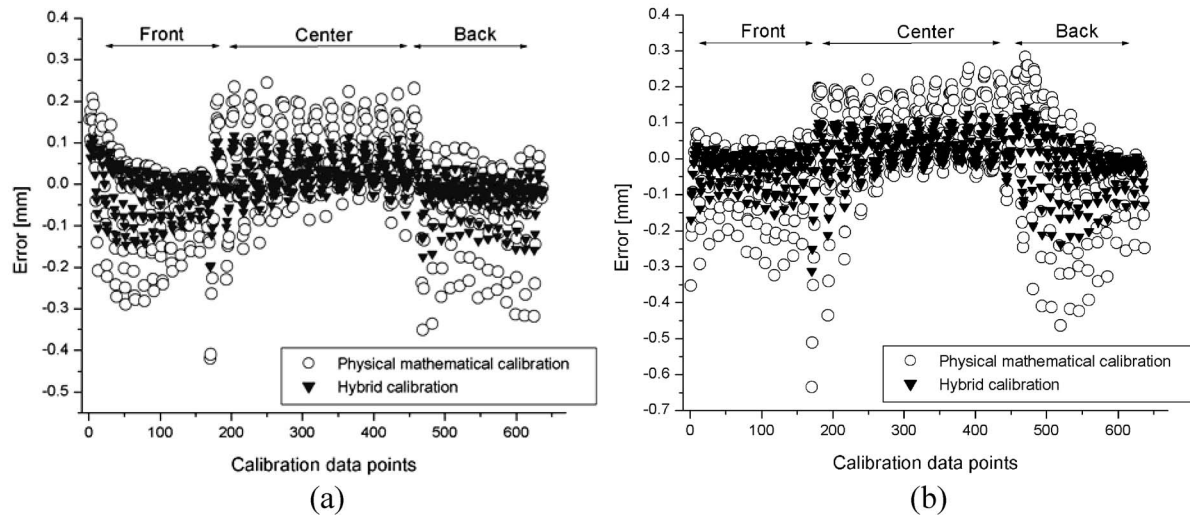


**Fig. 5** Comparison of calibration errors between the PMM and the hybrid method: (a) X position errors and (b) Y position errors.

BP neural network is ready to be employed. There is no certain rule for choosing the number of neurons in the hidden layer. In general, fewer neurons in the hidden layer make it difficult for the network to converge during training. The small number of hidden layer neurons may also cause the network to be sensitive to input deviation due to inaccurate centroid determination of markers. On the other hand, too many hidden neurons make the network too complex to be trained. It may take excessive time to learn from the samples. To achieve a high recognition rate as well as a reasonable learning speed, eight neurons were chosen for the hidden layer, as indicated. For programming implementation of the neural networks, a system that was customized by the authors was employed.

#### 4 Calibration Results of the Hybrid Method

After defining the PMM, that is, after finding the values for the 25 coefficients of the physical model, the performance of the hybrid calibration method was experimentally tested. The experimental setup employed was the same as that for the PMM testing, as shown in Figs 4(a) and 4(b), except that more marker images were collected for a total of 637 data points. Among these, 100 reference marker-image pairs were deployed to train the neurons. That is, the 2-D image centroids and the corresponding 3-D positions were used as the input and the target output of the neural network, respectively. Since the system is nonlinear, the initial assignment of connection weights is important to the training results. Initially, the connection weights were arbitrarily assigned from zero to one.

After training the network, the initial 3-D positions of  $(X', Y', Z')$ , which can be calculated by the PMM, were presented to the network to find the corrections of  $(\Delta X, \Delta Y, \Delta Z)$ . Figures 5 and 6 show the patterns of calibration errors for all of the 637 data points for both of the cases: that is, direct results from the PMM and the effects of the hybrid calibration. The errors correspond to the deviations from accurate positions  $(X, Y, Z)$  of markers on the calibration plate. For example, the X position error is  $(X$

$-X')$  for the PMM and  $(X - X' - \Delta X)$  for the hybrid calibration, respectively. As shown in Fig. 4, the calibration plate was placed at three different locations in collecting data. The marker data points corresponding to these locations are indicated in the plots. The hybrid approach clearly exhibits recognizable trends in error reduction for all X, Y, and Z components. Figures 5 and 6 indicate that the neural network had more pronounced effects on minimizing larger errors that had been generated by the PMM. These larger errors appear to be systematic rather than random. The error reduction of the X and Y components is very similar in behavior. Note that the data points, which were used as reference values in the calibration process and here for assessing errors, have some uncertainty of  $\pm 0.1$  mm in spacing since the calibration plate could not be fabricated with exact precision, as previously indicated. When this uncertainty is considered, the calibration results are very satis-

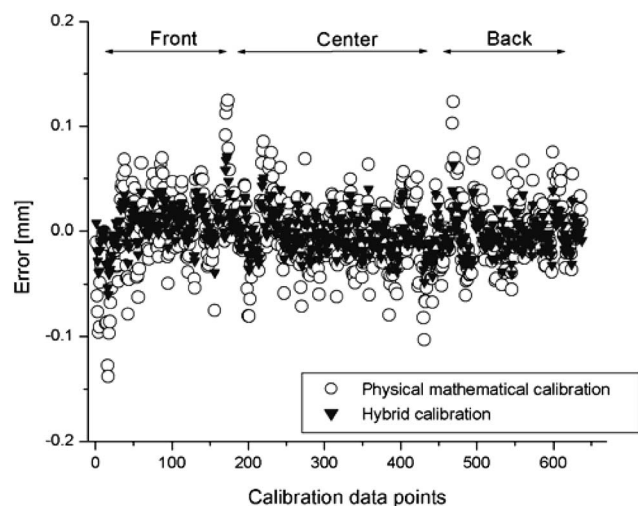


**Fig. 6** Comparison of calibration errors between the PMM and the hybrid method for Z position errors.

factory. The  $X$  and  $Y$  components have greater errors than the  $Z$  position, as expected, since the latter could be captured by the both cameras.

The average errors of those data points shown in Figs. 5 and 6 are 0.082 and 0.058 mm for the  $X$  component, 0.100 and 0.070 mm for the  $Y$  component, and 0.028 and 0.022 mm for the  $Z$  component, respectively. The average error was reduced about 30% for the  $X$  and  $Y$  components. It is about 22% for the  $Z$  component. The reduction of the

$Z$  component error is less pronounced in absolute value as compared with the  $X$  and  $Y$  errors. This can be due to the better uncertainty in the measurement. We believe that the average performance of the hybrid method reached a limit primarily due to the uncertainty in the spacing of reference markers and it can be further enhanced with a more accurate calibration plate. To judge the overall performance of the hybrid calibration, the average distance error was defined as follows:

$$\text{average error} = \frac{\left[ \sum_{i=1}^N (X_i - X'_i - \Delta x)^2 + (Y_i - Y'_i - \Delta y)^2 + (Z_i - Z'_i - \Delta z)^2 \right]^{1/2}}{N}, \quad (11)$$

where  $N$  is the number of data points. Figure 7 shows the distance errors, that is, square roots of individual terms in Eq. (16), for both of the approaches. Similar to the trends in Figs. 5 and 6, the neural network could substantially reduce the errors with large deviations. The ability of the hybrid method to reduce larger errors can be an asset in real applications. The average distance errors are 0.21 mm for the PMM and 0.14 mm for the hybrid calibration, respectively, which correspond to about a 33% reduction. The latter is very close to the uncertainty of the marker spacing on the calibration plate.

## 5 Conclusion

A hybrid calibration technique was developed for 3-D stereoscopic imaging, by combining a PMM with artificial neural networks. The strategy is to exploit the merits of the two approaches while reinforcing their weaknesses. Various

factors can contribute to the uncertainty in 3-D stereoscopic vision. The most important contributors can be imaging lens aberration and misalignment of the optical components, which can induce systematic errors. The imperfection of the PMM can also cause errors in stereoscopic system calibration. Based on computer simulation of experiments and real testing, the hybrid method is effective in dealing with the aforementioned systematic errors. Especially, the neural network approach could reduce larger errors, that is, outliers in experimental data. Our experimental investigation demonstrates that the accuracy in predicting the 3-D coordinates from 2-D projection image pairs can be improved by about 30% with the hybrid method as compared with the pure PMM. The uncertainty of the hybrid method in the current study approached the uncertainty of the reference values employed for comparison. In the future, when more precise calibration markers are utilized as the reference, the calibration errors can be reduced further. The concept of reinforcing PMMs by adding artificial neural networks appears to be promising in stereoscopic imaging. Our approach here is believed to be also applicable to other areas of 3-D vision for various applications.

## Acknowledgment

This work has been supported by the National Aeronautics and Space Administration (NASA) Grant No. NAG 8-1248. The authors also greatly appreciate the assistance of Dr. Yi Ge in conducting the experiments.

## References

1. Y. Ge and S. S. Cha, "Application of neural networks to stereoscopic imaging velocimetry," *AIAA J.* **38**(3), 487–492 (2000).
2. O. J. Fakhoury, "Experimental study of stress analysis using stereoscopic speckle-tracking photogrammetry compared to other conventional methodology," PhD Dissertation, the University of Illinois at Chicago (2005).
3. R. Y. Tsai, "A versatile camera calibration technique for high accuracy 3-D machine vision metrology using off-the-shelf TV cameras and lenses," *IEEE J. Rob. Autom.* **Ra-3**, 323–344 (1987).
4. J. Weng, P. Cohen, and M. Herniou, "Calibration of stereo cameras using a nonlinear distortion model (CCD sensory)," in *Proc. 10th Int. Conf. Pattern Recognition*, Vol. **1**, 246–253 (1990).
5. W.-C. Choi and Y. G. Guezennec, "In-situ calibration for wide-angle, three-dimensional stereoscopic image analysis," *Appl. Opt.* **36**(29),

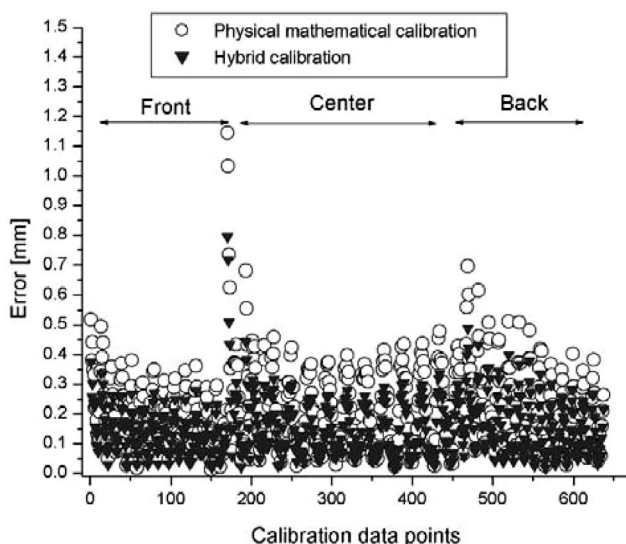


**Fig. 7** Comparison of distance errors in position between the PMM and the hybrid method.

- 7364–7373 (1997).
6. M. D. Betha, J. A. Lock, P. Crouser, and F. Merat, “A 3-D camera calibration technique stereo imaging velocimetry experiments,” *Opt. Eng.* **36**(12), 3445–3454 (1997).
  7. B. D. Ripley, *Pattern Recognition and Neural Networks*, Cambridge University Press, Cambridge (1996).



development, and pipeline integrity management.

**David J. Lee** received his BS degree in mechanical engineering from Dong-Guk University, South Korea, in 1996 and his MS and PhD degrees in mechanical engineering in 2001 and 2005, respectively, both from the University of Illinois at Chicago. Dr. Lee is currently a research engineer with the Gas Technology Institute. His research interests are nondestructive measurement of natural gas pipeline distribution and operation systems, pipeline coating test and



spectroscopy) for measurements of mechanical phenomena.

**Soyoung S. Cha** received his PhD degree in mechanical engineering from the University of Michigan in 1980 and was a research engineer with Northrop Corporation for the next 5 years. He then joined the Department of Mechanical and Industrial Engineering at the University of Illinois at Chicago as a faculty member in 1984. Dr. Cha's research interests are the application of optical techniques (interferometry, vision technology, holography, light scattering, and